Check for updates

Drivers of ocean warming in the western boundary currents of the Southern Hemisphere

Junde Li ✉, Moninya Roughan ✉ and Colette Kerry

Western boundary currents (WBCs) of the Southern Hemisphere transport heat poleward and are regions of rapid ocean warming. However, the mechanisms responsible for the enhanced warming over the Southern Hemisphere WBC extensions are still debated. Here we show that enhanced eddy generation in the WBC extensions through changes in barotropic and baroclinic instabilities results in enhanced ocean warming as the eddies propagate. This results from a poleward shift of the WBCs, associated with changes in the mid-latitude easterly winds. Consequently, the WBCs have penetrated poleward but not strengthened and are now transporting more heat into their extensions. Our study clearly elucidates the dynamic processes driving increased eddying and warming in the Southern Hemisphere WBC extensions and has implications for understanding and predicting ocean warming, marine heatwaves and the impact on the marine ecosystem in the WBC extensions under climate change.

Changes to the subtropical western boundary currents (WBCs, the western branch of the subtropical ocean gyres[1]) are driving a redistribution of heat globally, resulting in many changes, for example to local weather patterns, including rainfall[2], ocean carbon uptake[3] and marine heatwaves[4]. The changes occurring in the WBCs have been investigated in the Northern Hemisphere[5–7] and several studies have also focused on the changes in the WBCs of the Southern Hemisphere (SH)[1,8,9]. The three major subtropical WBCs of the SH are the Agulhas Current (AC) in the Indian Ocean, the East Australian Current (EAC) in the Pacific Ocean and the Brazil Current (BC) in the Atlantic Ocean, which are connected by the SH super gyre[10]. Over recent decades, surface ocean warming rates along the path of the SH WBCs have been shown to be two to three times greater than the global mean[6]. However, while it has been shown that the warming trends are non-uniform in the WBCs[11], the mechanisms driving the non-uniform warming trends are still under strong debate. For example, early study[6], primarily based on reanalysis data, proposed that the enhanced warming is probably driven by intensifying and/or poleward shifting of the WBCs, while multimodel (mostly coarse resolution) ensemble simulations suggest that the WBCs are both intensifying and shifting poleward under global warming[7]. Interestingly, in situ and satellite altimeter measurements over the Indian Ocean indicate that the AC is broadening as a result of more eddy activity[12]. The SH WBCs interact strongly with the Antarctic Circumpolar Current (ACC) and its associated circumpolar fronts without any inhibition by land south of the subtropical ocean gyres, especially in the AC and BC[13]. The convergence of warm and cold water at the southern boundary of the SH WBCs creates strong gradients in water properties, where biological productivity and the exchange of gasses and heat are enhanced[14]. Hence, investigating the ocean warming in the SH WBCs is crucial for understanding changes to global ocean heat transport and marine ecosystem.

The Southern Annular Mode (SAM), defined as the difference in the zonal mean sea level pressure between 40° S and 65° S (ref. [15]), is the leading mode of extratropical climate variability in the SH[16] that describes the (non-seasonal) north–south movement of the high-latitude westerly winds. The positive SAM phase is associated with a poleward shift in the high-latitude westerly winds[17,18]. Due to Antarctic stratospheric ozone depletion and increasing CO_2, the SAM has displayed positive trends over the recent decades[19,20], contributing to the spin-up of SH super gyres[21]. The SH subtropical gyres are primarily driven by basin-scale positive wind stress curl[1,18,22]. In response to global warming, the extratropical atmospheric surface winds have shifted toward higher latitudes and driven the poleward shift of the major ocean gyres[7,23]. The interannual variability in the EAC volume transport is tied to the SAM[24]; however, we know little about the impact of positive SAM trends on the transport trends of the SH WBCs.

Eddies are the weather systems of the ocean and WBC extensions are among the most eddy-rich regions of the planet with high eddy kinetic energy (EKE), showing a notable increase in mesoscale variability of 2–5% per decade[11]. In the SH, the poleward shift of the WBCs has increased the EKE trends in the Agulhas leakage[25,26], the EAC southern extension[27,28] and the Brazil–Malvinas Confluence (BMC)[29]. In the EAC, it has been shown that the EKE trends are non-uniform along the path of EAC, corresponding to non-uniform trends in sea surface temperature (SST)[27] and ocean heat content[28]. Examining the mechanism responsible for the non-uniform EKE trends may be beneficial to understand what drives the warming trends in the SH WBC extensions; however, to date, it remains unresolved.

In this study, we first show the non-uniform trends of SST and EKE in the SH using the latest 28-yr (1993–2020) satellite observations. Then, we uncover the dynamical mechanism responsible for the increasing EKE trends in the SH WBCs from a high-resolution ocean reanalysis. Finally, we explore the drivers of the poleward shift of the SH WBCs. In this way, we demonstrate the link from changes in the SH wind fields (positive SAM trends) to a poleward shift in the southern boundary of the subtropical ocean gyres, increased heat transport and eddy activity driven ocean warming in the WBC extensions.

Ocean warming trends are related to eddy activity

Over the past three decades, the SST observations show statistically significant warming trends across the entire SH north of 60° S

School of Biological Earth and Environmental Sciences, University of New South Wales, Sydney, New South Wales, Australia. ✉e-mail: junde.li@unsw.edu.au; mroughan@unsw.edu.au
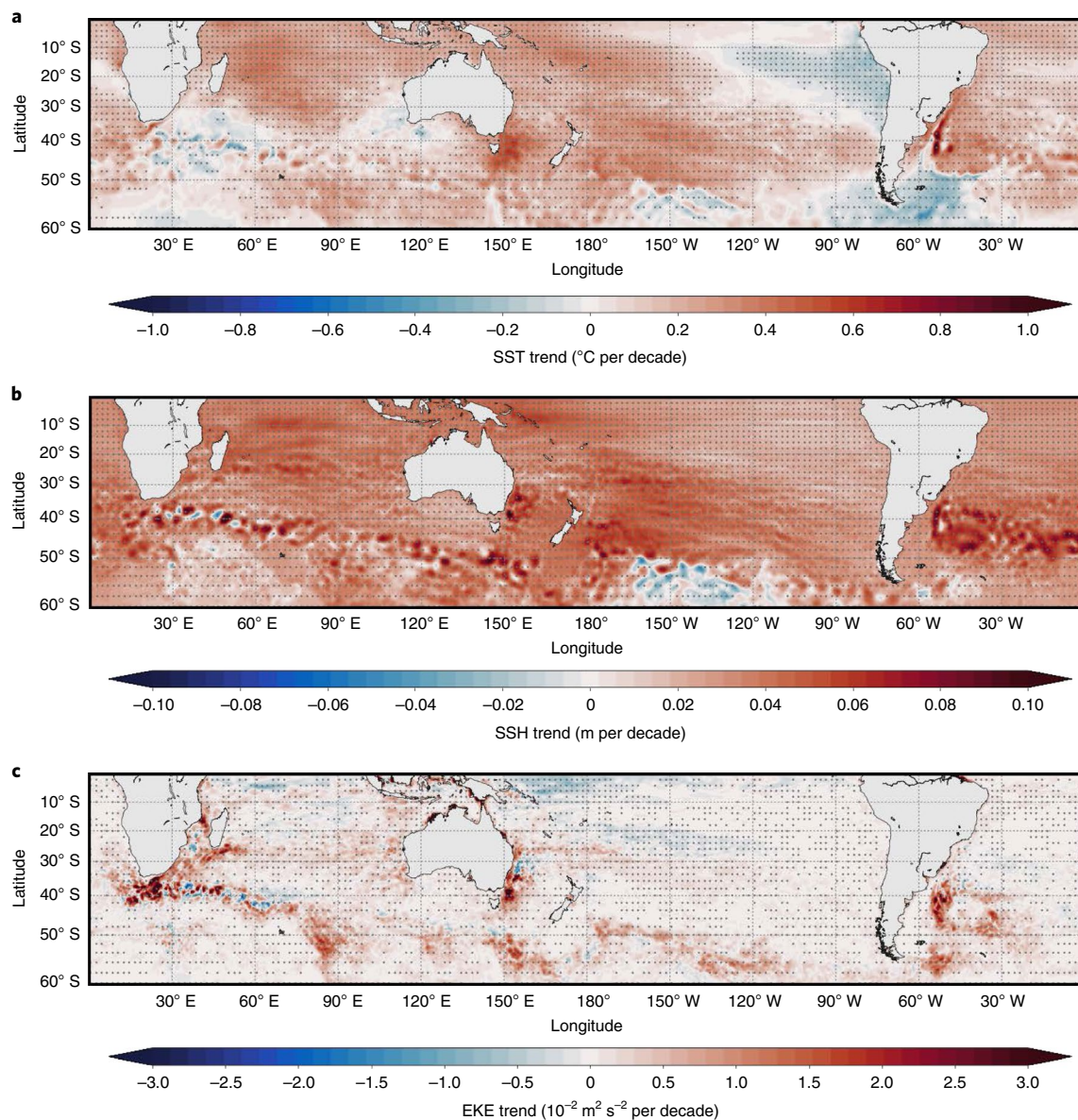
Fig. 1 | Linear SST, SSH and surface EKE trends from observations in the SH. a, Spatial distribution of SST trends between 1993 and 2020. **b,c**, Same as **a** but for the SSH (**b**) and EKE (**c**). The grey stippling indicates that the trends are statistically significant above the 95% confidence level.

(except the tropical southeast Pacific Ocean and south of the BMC) (Fig. 1a), implying that the global ocean has experienced notable warming with a proportion of that attributed to anthropogenic climate change. The largest warming trends can be observed in the WBC extension regions, particularly in the Agulhas Retroflection regions, the EAC southern extension and the BMC regions. We also find elevated sea surface height (SSH) trends over the entire SH (Fig. 1b)[21], except in the high-latitude central Pacific Ocean (50°S to 60°S). Consistent with the SST trends, the rates of sea level rise are higher than the mean in the Agulhas Retroflection regions, the EAC southern extension and the BMC regions and the statistically significant positive EKE trends in these regions are also much higher than the other regions (Fig. 1c).

To resolve the dynamical connection between ocean warming and mesoscale eddy activity in the SH WBCs, we first show the observed spatial patterns of surface mean kinetic energy (MKE), EKE and SST in these regions. Strong, energetic, narrow and fast WBCs transport warm waters poleward along the western boundary of the three ocean basins (Extended Data Figs. 1a–c and 2a–c).

Large anticyclonic eddies trap warm water as they shed from the main WBC jets and propagate further southwestward[30–33] while the WBCs separate from the coast turning eastward. The poleward penetration of eddies results in high EKE and enhanced ocean warming in the WBC extensions (Fig. 2a–c and Extended Data Fig. 1g–i).

We demonstrate that changes in SST and EKE along the path of the three SH WBCs are non-uniform, as shown in the satellite observations (Fig. 1a). We find the largest positive SST trends in their downstream extensions (Fig. 2a–c). Consistent with SST, non-uniform EKE trends are also observed in the WBCs, with the largest increasing EKE trends in the WBC extensions but with only weak positive EKE trends in the upstream WBC jets (Fig. 2d–f). We even find significant negative EKE trends upstream of the EAC typical separation region (Fig. 2e), where EKE is the strongest (Extended Data Fig. 1h), indicating a decrease in eddy activity in this region[28]. The non-uniform trends of SST and EKE are concomitant in the WBC extensions, implying that the ocean warming trends are associated with the increasing mesoscale eddy activity.
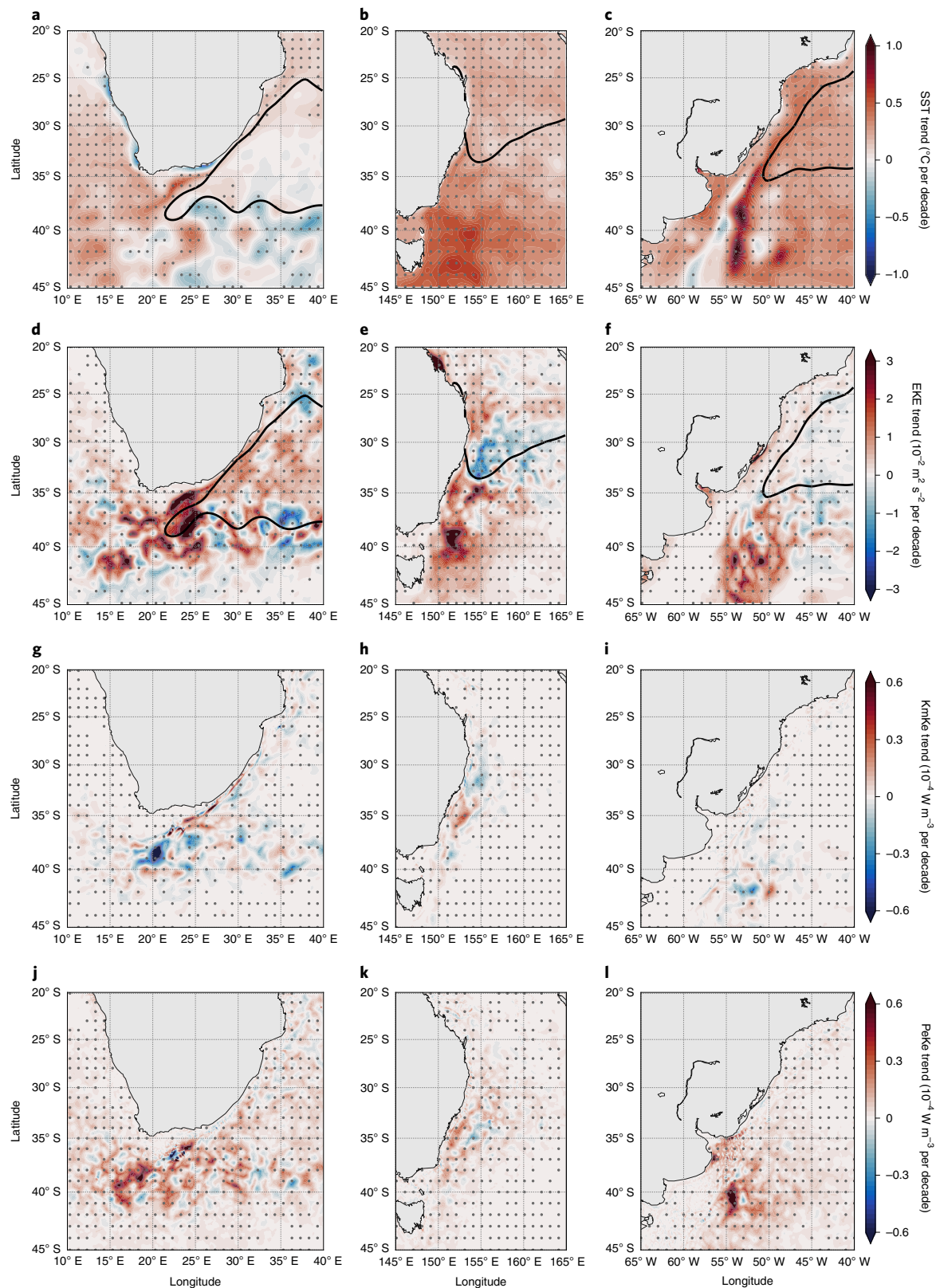
Fig. 2 | Linear SST, surface EKE, KmKe and PeKe trends in the SH WBCs. a, Spatial distribution of observed SST trends between 1993 and 2020 in the AC system. The black line indicates the 0.9 m contour of climatological mean SSH (1993–2020) from AVISO. **b**,**c**, Same as **a** but for the EAC (**b**) and BC (**c**), except the black line in **c** indicates the 0.6 m contour of climatological mean SSH from AVISO. **d**–**f**, Same as **a**–**c** but for the observed EKE trends. **g**–**l**, Same as **a**–**c** but for the trends of barotropic (KmKe) (**g**–**i**) and baroclinic (PeKe) (**j**–**l**) energy conversion from BRAN over the upper 1,000 m, respectively. In all panels, the grey stippling indicates that the trends are statistically significant above the 95% confidence level.
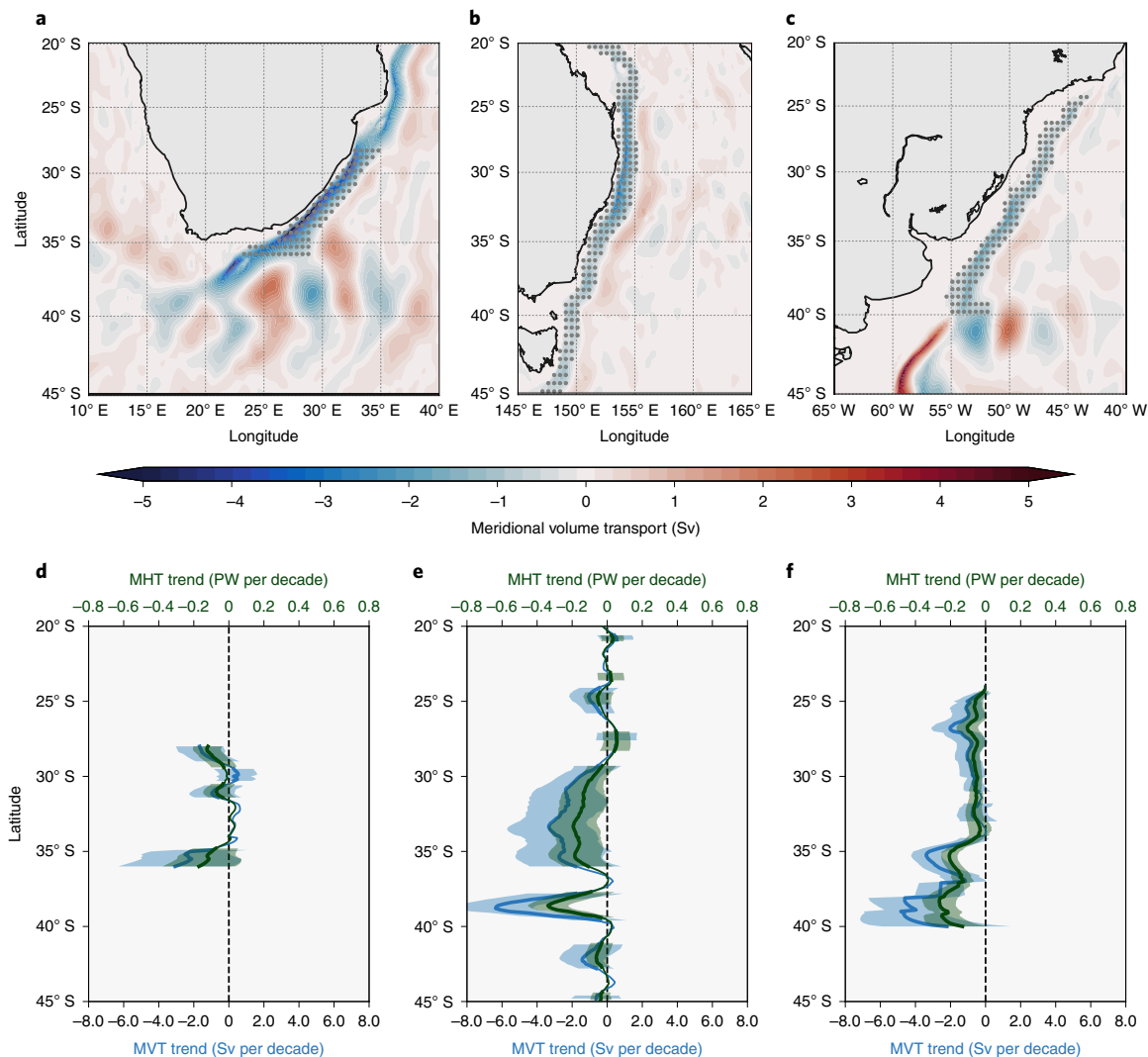
Fig. 3 | Mean and linear trends of meridional transport in the SH WBCs. a, Spatial distribution of mean MVT averaged over the upper 1,000 m in the AC system from BRAN reanalysis. The grey stippling regions indicate regions used to calculate the linear trends of meridional transport along the AC path. **b,c**, Same as **a** but for the EAC (**b**) and BC (**c**). **d**, Linear meridional transport trends between 1993 and 2020 along the AC path. Thin blue and green lines indicate the trends of meridional volume and heat transport, respectively. Thick line and shading indicate the trends that are statistically significant above the 95% confidence level and the standard errors. Negative trend means increasing poleward. **e,f**, Same as **d** but for the EAC (**e**) and BC (**f**).

Now, we examine what physical processes are responsible for the EKE sources and their changes in the SH WBCs. Barotropic instabilities result from horizontal shear in the WBC jet, feeding eddy growth by extracting kinetic energy from the unstable mean-flow field (KmKe)[34]. However, baroclinic instabilities are associated with the vertical shear, proportional to the horizontal temperature gradient, facilitating eddy growth by drawing energy from the eddy available potential energy (PeKe)[34]. Therefore, the stability of the mean flow and the horizontal temperature gradient become the key factors that impact EKE variability in the WBCs and their extensions, to varying degrees depending on the particular WBC.

To further elucidate the physical mechanisms responsible for the increasing EKE trends in the WBC extensions, we examine the primary sources of EKE from an eddy-resolving (10 km resolution) and data-assimilating ocean reanalysis BRAN[35]. We choose this product because it represents the SH WBCs well and resolves mesoscale eddies with similar spatial distributions of surface MKE (Extended Data Fig. 1a–f) and EKE (Extended Data Fig. 1g–l) in the SH WBCs compared to observations, which are crucial components of the global heat transport[36]. The surface energy of the WBCs and

mesoscale eddies in the high-resolution reanalysis agree well with the satellite observations (Extended Data Fig. 1), giving us the confidence to use the eddy-resolving reanalysis to calculate the energy conversion terms (KmKe and PeKe) in the WBC systems.

In the core of the AC jet, we find strong positive energy conversion from MKE to EKE through barotropic instabilities of the mean flow (KmKe) (Extended Data Fig. 3a) and weak energy conversion from eddy available potential energy to EKE due to baroclinic instabilities (PeKe) (Extended Data Fig. 3d). To the west of the Agulhas Retroflection regions, although baroclinic instabilities contribute to the EKE variability, barotropic instabilities (KmKe) dominate the energy conversion (Extended Data Fig. 3a,d), consistent with previous studies[37,38]. Strong KmKe indicates that the mean flow is unstable and transfers the kinetic energy to the eddy field in these regions, where the strong temperature gradients (Extended Data Fig. 2d) also lead to the large PeKe and contribute to the energy conversion from eddy available potential energy to EKE (Extended Data Fig. 3d). These energy conversion terms are also showing changes. The spatial distributions of trends in KmKe and PeKe indicate that the increasing EKE trends are mainly sourced from the
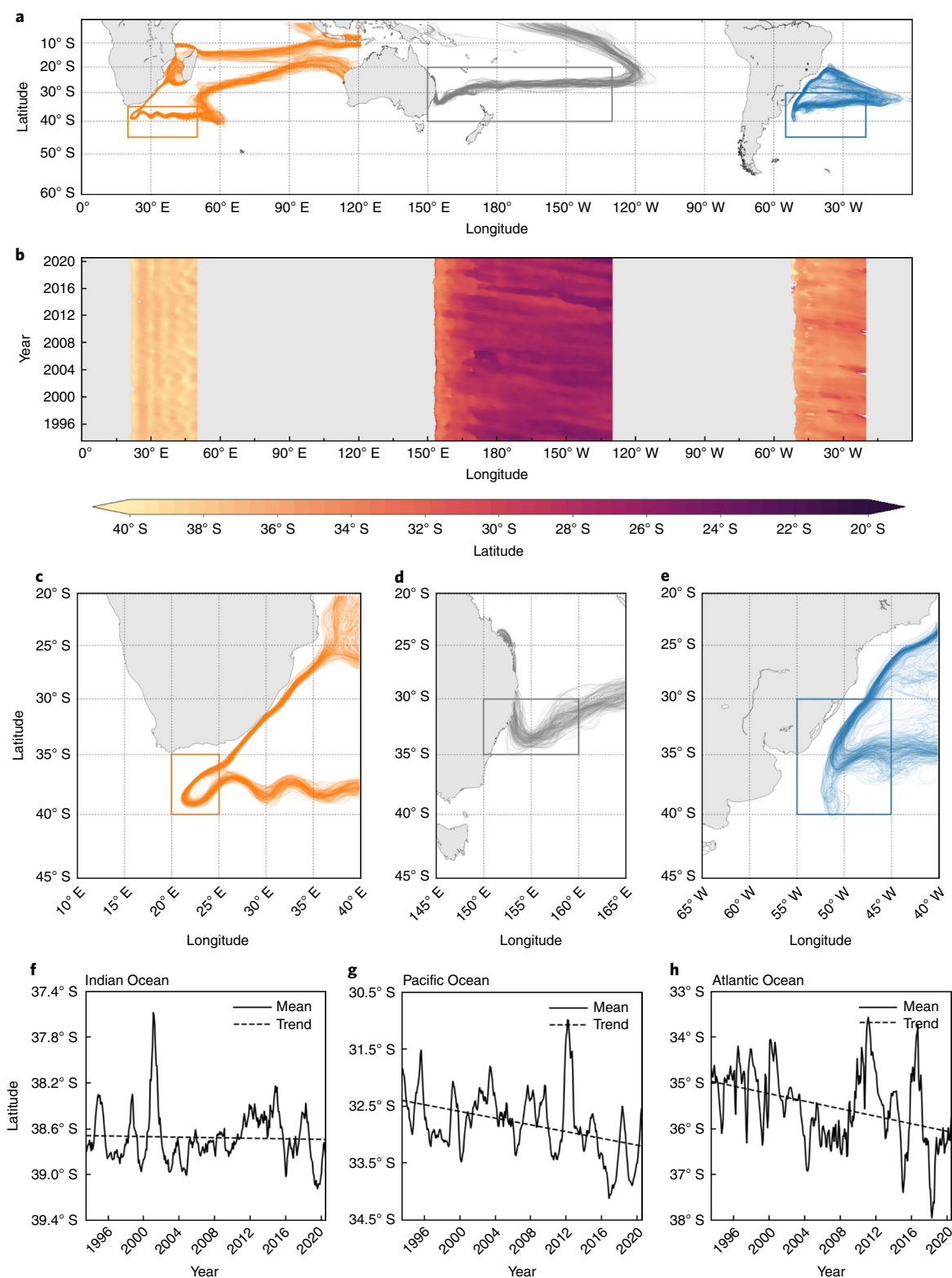
Fig. 4 | Illustration and trends of subtropical ocean gyres in the SH. a, Monthly mean SSH contours represent the boundaries of subtropical gyres from AVISO (1993–2020). The orange lines in the Indian Ocean and the grey lines in the Pacific Ocean indicate the 0.9 m contours. The blue lines in the Atlantic Ocean indicate the 0.6 m contours. The orange, grey and blue boxes indicate the southern boundaries of subtropical gyres in each ocean basin. **b,** Monthly latitudinal variations of the southern boundaries of subtropical gyres. **c,** Monthly mean SSH contours represent the AC. The orange box indicates the AC separation region. **d,e,** Same as **c** but for the EAC (**d**) and BC (**e**) separation regions. **f,** Time series of zonal mean latitudes over the AC separation region. The dashed line indicates the linear trend. **g,h,** Same as **f** but for the EAC (**g**) and BC (**h**) separation regions.
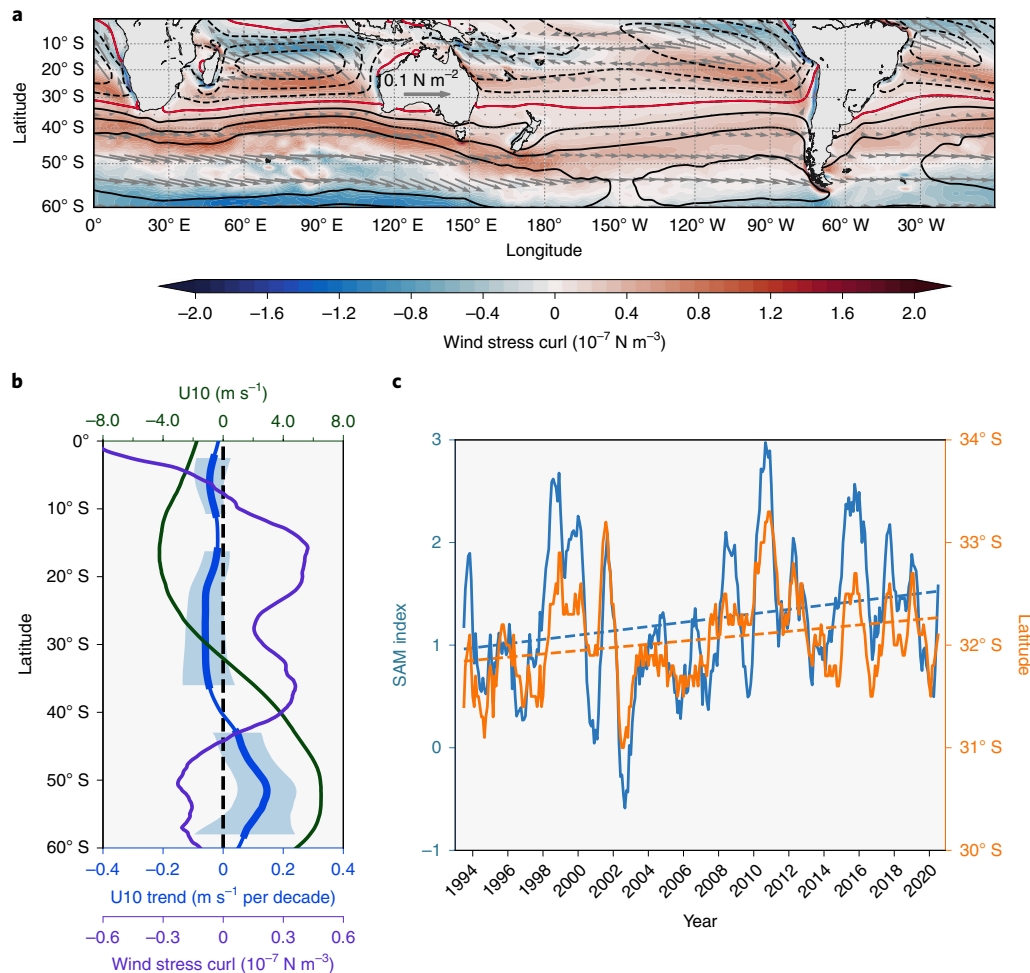
Fig. 5 | Large-scale wind pattern and trends associated with SAM. a, Large-scale climatological mean winds from ERA5. The shading shows wind stress curl. The grey vectors indicate the wind stress, with solid (dashed) black contours representing the westerly (easterly) winds and the solid red line denotes the zero wind stress. **b**, Zonal mean ocean surface winds at 10 m (U10) over the SH. The purple line, green line and blue line indicate the zonal mean climatological wind stress curl, U10 and the trends of zonal mean U10, respectively. Thick blue line and blue shading indicate the trends of zonal mean U10 that are statistically significant above the 95% confidence level and the corresponding standard errors. **c**, Time series of zonal mean latitudes of the zero wind stress (solid orange line) and SAM index (solid blue line). The dashed orange line and blue line indicate the linear trends of zonal mean latitudes of zero wind stress and SAM index, respectively.

baroclinic instabilities (Fig. 2g,j) west of the Agulhas Retroflection regions, which are associated with the positive trends of temperature gradients (Extended Data Fig. 2g).

In the South Pacific Ocean, eddy generation in the EAC separation region is dominated by barotropic instabilities (Extended Data Fig. 3b)[39]. The highest EKE and KmKe are located north of 35° S (Extended Data Figs. 1h,k and 3b), whereas there is a poleward shift of the locations in the strongest trends of EKE and KmKe (Fig. 2e,h), implying that more eddies are forming further south. Without strong temperature gradients, the energy conversion from eddy available potential energy to EKE through the baroclinic instabilities is relatively weak in the EAC typical separation region (Extended Data Fig. 3e) but we find significant increasing trends of the baroclinic energy conversion and temperature gradients further downstream in the EAC southern extension, particularly closer to the coast (Fig. 2k and Extended Data Fig. 2h).

In contrast, baroclinic instabilities dominate the variability of EKE in the BMC region (Extended Data Fig. 3f), associated with the strong horizontal temperature gradient (Extended Data Fig. 2f). Previous studies have also shown the dominant role of the baroclinic instabilities along the BC path between 20° S and 36° S (ref. [40]),

particularly in the Rio Grande Cone region (30° S to 35.5° S)[41]. The positive trends in temperature gradients have resulted in increased baroclinic instabilities over recent decades (Fig. 2l and Extended Data Fig. 2i). However, the barotropic instabilities are largely negligible in this region (Extended Data Fig. 3c) without increasing trends (Fig. 2i).

Poleward shift of WBCs increases eddy activity

To further elaborate on the important changes occurring in the SH WBCs, we show the patterns (Fig. 3a–c) and trends (Fig. 3d–f) in meridional (poleward) volume and heat transport along the path of the WBCs, which have similar latitudinal patterns. There are no statistically significant meridional transport trends in the upstream regions of the three SH WBCs, that is where MKE is high relative to EKE (Extended Data Fig. 1), implying that the WBCs have not strengthened over the past decades, consistent with previous studies in the AC[12], EAC[28,42] and BC[43,44]. However, we find statistically significant increasing trends of meridional volume transport (MVT) and heat transport in the WBC poleward extensions, particularly in the EAC and BC (Fig. 3e,f), suggesting that the WBCs have penetrated poleward and are transporting more heat into their
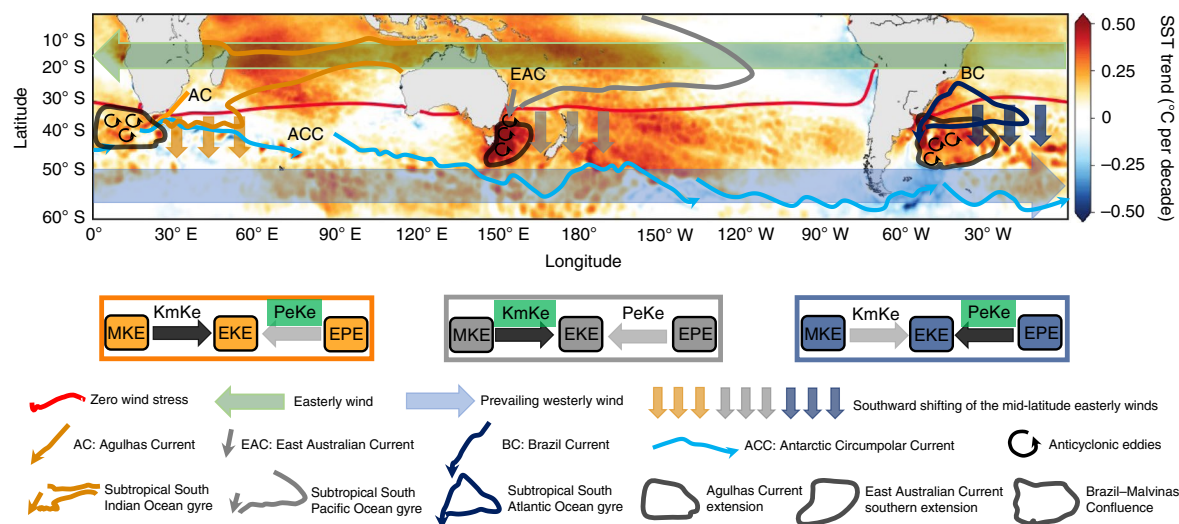
Fig. 6 | Schematic diagram of the mechanisms driving ocean warming in the SH WBC extensions. The schematic is overlaid on the decadal SST trend (1993–2020). The thick red line indicates the mean zero wind stress. The vertical orange, grey and blue arrows illustrate the southward shifting of the mid-latitude easterly winds. The orange, grey, blue and cyan curves with the arrows denote the AC, EAC, BC and ACC, respectively. The middle three panels show the main sources of EKE (black arrows) and the dominant trends (green shading) of energy conversions in each of the SH WBC extensions. EPE represents the eddy available potential energy. In response to the positive SAM trend, a poleward shift of the mid-latitude easterly winds results in a shift in the southern boundary of the subtropical ocean gyres, driving the increased eddying and ocean warming in the SH WBC extensions.

southern extensions. This is because weak WBCs are more barotropically stable and can retain more energy to penetrate further south and transport more warm water poleward[28,39].

Now, we show the link between the increasing meridional transport and the trends of KmKe and PeKe in the SH WBC extensions. We find statistically significant positive trends of KmKe after the intensified AC separates from the coast between 35° S and 36° S (Fig. 2g). The subpolar front is located south of the AC region; more heat transported into this cold region enhances the horizontal temperature gradient (Extended Data Fig. 2g), resulting in the increasing trends in PeKe (Fig. 2j).

In the EAC southern extension, where the meridional transport has increased (Fig. 3e), we find a significant increasing trend of KmKe between 35° S and 36° S (Fig. 2h). However, we do not find significant increasing trends of KmKe south of 37° S. This is probably because the mean flow is weak in this region. Although the horizontal temperature gradient is not strong in the EAC southern extension (Extended Data Fig. 2e), intensified meridional transport can increase the PeKe due to the increased horizontal temperature gradient (Fig. 2k and Extended Data Fig. 2h), contributing to the eddy generation. This is consistent with a previous study, which suggests that the SST variability in the EAC southern extension is connected to the stability of the thermocline and low-frequency variability of baroclinic disturbances in the Tasman Sea[42].

Compared to the AC and EAC, the BC is the weakest (Extended Data Fig. 1a–c). Although the meridional transport has increased south of 35° S, we do not find a significant increasing KmKe trend (Fig. 2i) because a weak mean flow tends to be relatively stable[39]. The northward Malvinas Current brings cold water from the ACC to the BMC region, forming a large horizontal temperature gradient (Extended Data Fig. 2f). Increased poleward meridional transport south of 35° S further enhances the horizontal temperature gradient (Extended Data Fig. 2i). As a result, we find statistically significant PeKe trends in the BMC region (Fig. 2l).

Mechanism for the subtropical ocean gyres poleward shift
The poleward penetration of the SH WBCs is associated with the poleward shift of the subtropical gyres. To show the variability in

the location of the subtropical gyres, we first remove the sea level trend averaged over the entire SH (0° S to 60° S) from the original SSH observations and then choose the monthly mean SSH to represent the position of the gyres[26,45]. The observed (detrended) SSH isolines capture the subtropical gyres well (Fig. 4a) and show the variations in their southern boundaries in each ocean basin, particularly in the WBCs (Fig. 4b). In each WBC system, the elevated SSH extends eastward to form the southern branch of the three subtropical gyres after separating from the western boundaries. To illustrate the poleward shift of the WBCs, we focus on the variability and trends of the WBC southern boundaries (Fig. 4c–e).

The southern boundary of the South Indian Ocean gyre has been remarkably stable over recent decades (Fig. 4b). The southward displacement of AC separation is small and not significant, with a trend of $-0.01 \pm 0.08°$ (1.37 ± 9 km) per decade ($P > 0.05$, Fig. 4f), in agreement with recent studies[23,26,46]. This is probably because it is proximal to the ACC, which acts as a stabilizing agent and is accelerating on its north flank due to ocean warming[47].

In the South Pacific Ocean, we find a large poleward shift of the EAC, with a trend of $-0.30 \pm 0.19°$ (33 ± 21 km) per decade ($P < 0.05$, Fig. 4g). This suggests that the EAC has penetrated ~92 km south during the past three decades. While an increased poleward extension has been shown[7,28,48–50], our results now quantify the rate of change in the WBCs, which are consistent with estimates of changes in the subtropical gyres from the SSH and SST observations[23].

As a branch of the ACC, the Malvinas Current flows northward along the continental slope of Argentina up to 38° S, which is the average location of BMC. Here we find that the BC has significantly shifted poleward at a rate of $-0.41 \pm 0.28°$ (46 ± 31 km) per decade ($P < 0.05$, Fig. 4h), which is similar to previous estimates in the BMC region showing a southward shifting rate of $-0.6°$ to $-0.9°$ per decade[9,45,51].

To examine the driver of the poleward shift of subtropical gyres, we show the spatial pattern of large-scale surface winds in the SH (Fig. 5a). Strong southeast trade winds dominate north of 30° S, whereas the prevailing westerly wind jet blows from west to east south of 30° S. This wind pattern forms a positive wind stress curl almost over the entire SH[52], particularly between 10° S and 45° S

(Fig. 5b), driving the anticyclonic subtropical gyres in each ocean basin. The zonal mean surface winds over the SH indicate that the strong easterly and westerly winds are between 10°S and 20°S and 40°S and 60°S respectively, with the zero zonal winds at ~32°S (Fig. 5b). In addition, we find significant increasing trends of the easterly winds between 20°S and 35°S and westerly winds south of 42°S (Fig. 5b). This not only shows that the high-latitude westerly winds have intensified but also indicates that the mid-latitude easterly winds have shifted poleward (Fig. 5c). It is worth noting that we do not find significant increasing trends in the easterly winds between 10°S and 20°S, where the zonal mean easterly winds are the strongest. This suggests that the easterly winds are shifting poleward but not strengthening; as a result, the subtropical ocean gyres and WBCs have shifted poleward. Therefore, the trends of meridional transport are non-uniform along the WBCs path (Fig. 3d–f), which are not statistically significant in the upstream regions but are increasing in the WBC extensions.

A negative zonal wind speed trend south of the zero zonal wind line (32°S) leads to a poleward shift of this line at a rate of −0.16 ± 0.16° per decade (Fig. 5c). Although it has been shown that the latitudinal location of the zonally averaged zero wind stress curl line is highly correlated with the SAM index[21], the zero wind stress curl line is located much further south than the separation latitudes of the WBCs (Figs. 4f–h and 5b). In contrast, the latitudinal location of the zonally averaged zero wind stress is more proximal to the southern boundary of subtropical ocean gyres (Figs. 4a and 5a). Therefore, we use the zero wind stress line in this study which describes the shift in both the easterly winds and the westerly winds. These changes in the mid-latitude easterly winds contribute to the poleward shift of the wind stress curl and the subtropical ocean gyres. Consequently, we observe a poleward shift of the southern boundary of the SH subtropical ocean gyres and WBCs (Fig. 4f–h).

SAM has displayed a remarkable increasing trend over the past decades[20]. Here we show that the increasing SAM is significantly correlated with a poleward shift of the mid-latitude easterly winds, with a correlation of 0.77 (above 95% significance level) between the SAM index and the latitudinal location of zonally averaged zero wind stress line (Fig. 5c). The high-latitude westerly winds have significantly strengthened rather than poleward shifted (Fig. 5b), which is in contrast to previous results showing the poleward shifting of high-latitude westerly winds[21] but showing similar patterns to an ensemble trend between 1979 and 2018 based on three atmospheric reanalysis[23]. Therefore, it is the poleward shift of the mid-latitude easterly winds that results in the poleward shift of the southern boundary of subtropical ocean gyres. This is not a strengthening of the WBCs but rather a poleward shift in the separation latitudes of WBCs.

Conclusions

Our findings clearly identify the dynamic mechanisms responsible for the enhanced warming over the SH WBC extensions. As summarized in the schematic diagram in Fig. 6, the easterly winds at mid-latitudes have shifted poleward associated with the positive SAM trends, resulting in a poleward shift of the southern boundaries of the three major SH ocean gyres. Our results show that the meridional heat transport (MHT) trends are non-uniform in the SH WBCs, where the greatest increases are in the WBC extensions but not in the upstream regions. This shows increased poleward penetration instead of strengthening or large upstream warming of the WBCs. We show that the increased meridional transport due to the poleward penetration of the WBCs carries more warm water into the WBC extensions. Significantly, we show the driving mechanism for increased eddy activity: an increase in eddy energy conversion through changes in the barotropic and/or baroclinic instabilities. These changes differ between the WBCs. For example: barotropic

instability trends dominate the increasing EKE in the EAC as the jet penetrates further south while baroclinic instability trends contribute most to the increased eddy activity in the AC and BC as the poleward penetration results in enhanced temperature gradients in their extensions. Although cyclonic eddies may make some contributions to the surface cooling, anticyclonic eddies dominate the WBC extensions. Increased anticyclonic eddy activity retains warm water from the WBCs that can propagate northwestward (AC) and poleward (EAC and BC), resulting in rapid ocean warming in the WBC extensions. Our results highlight the need for eddy-resolving datasets to better represent the dynamics of the SH WBCs and mesoscale eddies, which are crucial for understanding global heat transport. Our study elucidates the mechanisms driving ocean warming in the SH WBC extensions. While we have focussed on the SH, it is possible that our results provide insights into the drivers of changes occurring in the Northern Hemisphere WBCs as well. Hence, our results have far-reaching implications for understanding and predicting ocean temperature extremes in the world's major WBCs and the impact on marine ecosystems under climate change.

Online content

Any methods, additional references, Nature Research reporting summaries, source data, extended data, supplementary information, acknowledgements, peer review information; details of author contributions and competing interests; and statements of data and code availability are available at https://doi.org/10.1038/s41558-022-01473-8.

References

1. Hu, D. et al. Pacific western boundary currents and their roles in climate. *Nature* **522**, 299–308 (2015).
2. Shi, G., Ribbe, J., Cai, W. & Cowan, T. An interpretation of Australian rainfall projections. *Geophys. Res. Lett.* **35**, L02702 (2008).
3. Takahashi, T. et al. Climatological mean and decadal change in surface ocean pCO₂, and net sea-air CO₂ flux over the global oceans. *Deep-Sea Res. II* **56**, 554–577 (2009).
4. Behrens, E., Fernandez, D. & Sutton, P. Meridional oceanic heat transport influences marine heatwaves in the Tasman Sea on interannual to decadal timescales. *Front. Mar. Sci.* **6**, 228 (2019).
5. Kwon, Y.-O. et al. Role of the Gulf Stream and Kuroshio–Oyashio systems in large-scale atmosphere–ocean interaction: a review. *J. Clim.* **23**, 3249–3281 (2010).
6. Wu, L. et al. Enhanced warming over the global subtropical western boundary currents. *Nat. Clim. Change* **2**, 161–166 (2012).
7. Yang, H. et al. Intensification and poleward shift of subtropical western boundary currents in a warming climate. *J. Geophys. Res. Oceans* **121**, 4928–4945 (2016).
8. Holbrook, N. J., Goodwin, I. D., McGregor, S., Molina, E. & Power, S. B. ENSO to multi-decadal time scale changes in East Australian Current transports and Fort Denison sea level: oceanic Rossby waves as the connecting mechanism. *Deep-Sea Res. II* **58**, 547–558 (2011).
9. Lumpkin, R. & Garzoli, S. Interannual to decadal changes in the western South Atlantic's surface circulation. *J. Geophys. Res. Oceans* **116**, C01014 (2011).
10. Roemmich, D. et al. Decadal spinup of the South Pacific subtropical gyre. *J. Phys. Oceanogr.* **37**, 162–173 (2007).
11. Martínez-Moreno, J. et al. Global changes in oceanic mesoscale currents over the satellite altimetry record. *Nat. Clim. Change* **11**, 397–403 (2021).
12. Beal, L. M. & Elipot, S. Broadening not strengthening of the Agulhas Current since the early 1990s. *Nature* **540**, 570–573 (2016).
13. Imawaki, S., Bower, A. S., Beal, L. & Qiu, B. in *Ocean Circulation and Climate: A 21st Century Perspective* 2nd edn (eds Siedler, G. et al.) 305–338 (Academic Press, 2013).
14. Todd, R. E. et al. Global perspectives on observing ocean boundary current systems. *Front. Mar. Sci.* **6**, 423 (2019).
15. Marshall, G. J. Trends in the Southern Annular Mode from observations and reanalyses. *J. Clim.* **16**, 4134–4143 (2003).
16. Thompson, D. W. J. & Wallace, J. M. Annular modes in the extratropical circulation. Part I: month-to-month variability. *J. Clim.* **13**, 1000–1016 (2000).

17. Cai, W. Antarctic ozone depletion causes an intensification of the Southern Ocean super-gyre circulation. *Geophys. Res. Lett.* **33**, L03712 (2006).

18. Beal, L. M., Ruijter, W. P. M. D., Biastoch, A., Zahn, R. & SCOR/WCRP/IAPSO Working Group 136. On the role of the Agulhas system in ocean circulation and climate. *Nature* **472**, 429-436 (2011).

19. Cai, W., Whetton, P. H. & Karoly, D. J. The response of the Antarctic Oscillation to increasing and stabilized atmospheric CO₂. *J. Clim.* **16**, 1525–1538 (2003).

20. Fogt, R. L. & Marshall, G. J. The Southern Annular Mode: variability, trends, and climate impacts across the Southern Hemisphere. *WIREs Clim. Change* **11**, e652 (2020).

21. Qu, T., Fukumori, I. & Fine, R. A. Spin-up of the Southern Hemisphere super gyre. *J. Geophys. Res. Oceans* **124**, 154–170 (2019).

22. Cai, W., Shi, G., Cowan, T., Bi, D. & Ribbe, J. The response of the Southern Annular Mode, the East Australian Current, and the southern mid-latitude ocean circulation to global warming. *Geophys. Res. Lett.* **32**, L23706 (2005).

23. Yang, H. et al. Poleward shift of the major ocean gyres detected in a warming climate. *Geophys. Res. Lett.* **47**, e2019GL085868 (2020).

24. Zilberman, N. V., Roemmich, D. H. & Gille, S. T. Meridional volume transport in the South Pacific: mean and SAM-related variability. *J. Geophys. Res. Oceans* **119**, 2658–2678 (2014).

25. Biastoch, A., Böning, C. W., Schwarzkopf, F. U. & Lutjeharms, J. R. E. Increase in Agulhas leakage due to poleward shift of Southern Hemisphere westerlies. *Nature* **462**, 495–498 (2009).

26. Backeberg, B. C., Penven, P. & Rouault, M. Impact of intensified Indian Ocean winds on mesoscale variability in the Agulhas system. *Nat. Clim. Change* **2**, 608–612 (2012).

27. Malan, N., Roughan, M. & Kerry, C. The rate of coastal temperature rise adjacent to a warming western boundary current is nonuniform with latitude. *Geophys. Res. Lett.* **48**, e2020GL090751 (2021).

28. Li, J., Roughan, M. & Kerry, C. Variability and drivers of ocean temperature extremes in a warming western boundary current. *J. Clim.* **35**, 1097–1111 (2022).

29. Artana, C., Provost, C., Poli, L., Ferrari, R. & Lellouche, J.-M. Revisiting the Malvinas Current upper circulation and water masses using a high-resolution ocean reanalysis. *J. Geophys. Res. Oceans* **126**, e2021JC017271 (2021).

30. van Sebille, E. et al. Relating Agulhas leakage to the Agulhas Current retroflection location. *Ocean Sci.* **5**, 511–521 (2009).

31. Pilo, G. S., Oke, P. R., Rykova, T., Coleman, R. & Ridgway, K. Do East Australian Current anticyclonic eddies leave the Tasman Sea? *J. Geophys. Res. Oceans* **120**, 8099–8114 (2015).

32. Oke, P. R. et al. Revisiting the circulation of the East Australian Current: its path, separation, and eddy field. *Prog. Oceanogr.* **176**, 102139 (2019).

33. Schmidt, C., Schwarzkopf, F. U., Rühs, S. & Biastoch, A. Characteristics and robustness of Agulhas leakage estimates: an inter-comparison study of Lagrangian methods. *Ocean Sci.* **17**, 1067–1080 (2021).

34. Cushman-Roisin, B. & Beckers, J.-M. *Introduction to Geophysical Fluid Dynamics: Physical and Numerical Aspects* 2nd edn (Academic Press, 2011).

35. Chamberlain, M. A. et al. Next generation of Bluelink ocean reanalysis with multiscale data assimilation: BRAN2020. *Earth Syst. Sci. Data* **13**, 5663–5688 (2021).

36. Sen Gupta, A. et al. Future changes to the upper ocean western boundary currents across two generations of climate models. *Sci. Rep.* **11**, 9538 (2021).

37. Zhu, Y., Qiu, B., Lin, X. & Wang, F. Interannual eddy kinetic energy modulations in the Agulhas Return Current. *J. Geophys. Res. Oceans* **123**, 6449–6462 (2018).

38. Zhu, Y., Li, Y., Zhang, Z., Qiu, B. & Wang, F. The observed Agulhas Retroflection behaviors during 1993–2018. *J. Geophys. Res. Oceans* **126**, e2021JC017995 (2021).

39. Li, J., Roughan, M. & Kerry, C. Dynamics of interannual eddy kinetic energy modulations in a western boundary current. *Geophys. Res. Lett.* **48**, e2021GL094115 (2021).

40. Magalhães, F. C., Azevedo, J. L. L. & Oliveira, L. R. Energetics of eddy-mean flow interactions in the Brazil Current between 20° S and 36° S. *J. Geophys. Res. Oceans* **122**, 6129–6146 (2017).

41. Brum, A. L., de Azevedo, J. L. L., de Oliveira, L. R. & Calil, P. H. R. Energetics of the Brazil Current in the Rio Grande Cone region. *Deep-Sea Res. I* **128**, 67–81 (2017).

42. Sloyan, B. M. & O'Kane, T. J. Drivers of decadal variability in the Tasman Sea. *J. Geophys. Res. Oceans* **120**, 3193–3210 (2015).

43. Goes, M., Cirano, M., Mata, M. M. & Majumder, S. Long-term monitoring of the Brazil Current transport at 22°S from XBT and altimetry data: seasonal, interannual, and extreme variability. *J. Geophys. Res. Oceans* **124**, 3645–3663 (2019).

44. Chidichimo, M. P. et al. Brazil Current volume transport variability during 2009–2015 from a long-term moored array at 34.5° S. S. *J. Geophys. Res. Oceans* **126**, e2020JC017146 (2021).

45. Drouin, K. L., Lozier, M. S. & Johns, W. E. Variability and trends of the South Atlantic subtropical gyre. *J. Geophys. Res. Oceans* **126**, e2020JC016405 (2021).

46. Fadida, Y., Malan, N., Cronin, M. F. & Hermes, J. Trends in the Agulhas Return Current. *Deep-Sea Res. I* **175**, 103573 (2021).

47. Shi, J.-R., Talley, L. D., Xie, S.-P., Peng, Q. & Liu, W. Ocean warming and accelerating Southern Ocean zonal flow. *Nat. Clim. Change* **11**, 1090–1097 (2021).

48. Ridgway, K. R. Long-term trend and decadal variability of the southward penetration of the East Australian Current. *Geophys. Res. Lett.* **34**, L13613 (2007).

49. Hill, K. L., Rintoul, S. R., Ridgway, K. R. & Oke, P. R. Decadal changes in the South Pacific western boundary current system revealed in observations and ocean state estimates. *J. Geophys. Res. Oceans* **116**, C01009 (2011).

50. Cetina-Heredia, P., Roughan, M., Sebille, E. V. & Coleman, M. A. Long-term trends in the East Australian Current separation latitude and eddy driven transport. *J. Geophys. Res. Oceans* **119**, 4351–4366 (2014).

51. Combes, V. & Matano, R. P. Trends in the Brazil/Malvinas Confluence region. *Geophys. Res. Lett.* **41**, 8971–8977 (2014).

52. Chelton, D. B., Schlax, M. G., Freilich, M. H. & Milliff, R. F. Satellite measurements reveal persistent small-scale features in ocean winds. *Science* **303**, 978–983 (2004).

Methods

Observations and reanalysis. We use the latest daily Optimum Interpolation Sea Surface Temperature (OISST) v.2.1 to investigate the linear trend of SST. We calculate the energetic conversion terms from the daily Bluelink ReANalysis (BRAN) product. The monthly averaged surface winds at a height of 10 m from European Centre for Medium-Range Weather Forecasts (ECMWF) ERA5 atmospheric reanalysis were used to examine the large-scale variability of winds over the SH. The daily SSH satellite observations from Archiving, Validation and Interpretation of Satellite Oceanographic (AVISO) were used to calculate the daily surface geostrophic velocities:

$$u_g = -\frac{g}{f}\frac{\partial \eta}{\partial y} \qquad (1)$$

$$v_g = \frac{g}{f}\frac{\partial \eta}{\partial x} \qquad (2)$$

where η is the altimetric SSH, f is the Coriolis parameter, g is the gravitational acceleration of $9.81\,\mathrm{m\,s^{-2}}$ and x and y represent the zonal and meridional direction.

All the above datasets used in this study span 28 yr from January 1993 to December 2020, except the BRAN product. As BRAN2020 has not saved the vertical velocities before 1998 (ref. [35]), we use the BRAN2016 vertical velocities from 1994 to 1997 to fill this gap. The horizontal resolutions of OISST v.2.1, AVISO and ERA5 datasets are $0.25° \times 0.25°$. BRAN dataset has a high resolution of $0.1° \times 0.1°$, which can resolve the mesoscale eddies and associated dynamic processes in the global ocean (Extended Data Figs. 1 and 3).

Energetics metrics. To quantify the depth-dependent MKE, EKE and energy conversion terms, we calculate the following energetics metrics[53]:

$$\mathrm{MKE} = \frac{1}{2}(\overline{u}^2 + \overline{v}^2) \qquad (3)$$

$$\mathrm{EKE} = \frac{1}{2}(u'^2 + v'^2) \qquad (4)$$

$$\mathrm{KmKe} = -\rho_0\left[u'u'\frac{\partial \overline{u}}{\partial x} + u'v'\frac{\partial \overline{u}}{\partial y} + v'u'\frac{\partial \overline{v}}{\partial x} + v'v'\frac{\partial \overline{v}}{\partial y}\right] \qquad (5)$$

$$\mathrm{PeKe} = -g\rho'w' \qquad (6)$$

where $\overline{u}$ and $\overline{v}$ are the time-mean zonal and meridional velocity components over the whole time period (1993–2020), respectively. Statements $u' = u - \overline{u}$, $v' = v - \overline{v}$ and $w' = w - \overline{w}$ are the time-varying zonal, meridional and vertical velocity components, respectively. Parameter ρ_0 is the constant seawater density of $1,025\,\mathrm{kg\,m^{-3}}$ and ρ' is the perturbation of the seawater density.

The energy conversion terms KmKe and PeKe represent the energy transfer rate from MKE to EKE due to barotropic instabilities of the mean flow (KmKe) and from eddy available potential energy to EKE through the baroclinic instabilities (PeKe)[53,54]. The KmKe and PeKe are direct sources of EKE growth, with positive values indicating the eddy formation. In this study, we averaged KmKe and PeKe over the upper 1,000 m.

SST gradient and MHT analysis. The horizontal SST gradient, MVT and MHT are computed as follows:

$$\nabla \mathrm{SST} = \sqrt{\left(\frac{\partial \mathrm{SST}}{\partial x}\right)^2 + \left(\frac{\partial \mathrm{SST}}{\partial y}\right)^2} \qquad (7)$$

$$\mathrm{MVT} = \int_{x_1}^{x_2}\int_{-1,000}^{0} V(z)T(z)\mathrm{d}z\mathrm{d}x \qquad (8)$$

$$\mathrm{MHT} = \int_{x_1}^{x_2}\int_{-1,000}^{0} \rho C_p V(z)T(z)\mathrm{d}z\mathrm{d}x \qquad (9)$$

where ρ, C_p, $V(z)$ and $T(z)$ are the seawater density, specific heat capacity, meridional velocity component and temperature of seawater, respectively. Parameters x_1 and x_2 represent the western and eastern boundaries. MVT and MHT are calculated from 20° S to 45° S along the EAC path but from 28° S to 36° S in the AC and from 24° S to 40° S in the BC before they turn eastward and shed anticyclonic eddies.

Large-scale SSH and wind. To extract the large-scale monthly SSH and wind from the $0.25° \times 0.25°$ product, we use a spatial convolution with a constant $3° \times 3°$ kernel K and a 12-month running mean[11], defined as following:

$$\mathrm{SSH}_{\mathrm{ls}}(x, y, t) = \frac{\int\int \widetilde{\mathrm{SSH}}(x - x', y - y', t)K(x', y')\mathrm{d}x'\mathrm{d}y'}{\int\int K(x', y')\mathrm{d}x'\mathrm{d}y'} \qquad (10)$$

$$\vec{U}_{\mathrm{ls}}(x, y, t) = \frac{\int\int \widetilde{\vec{U}}(x - x', y - y', t)K(x', y')\mathrm{d}x'\mathrm{d}y'}{\int\int K(x', y')\mathrm{d}x'\mathrm{d}y'} \qquad (11)$$

where $\mathrm{SSH}_{\mathrm{ls}}$ and $\vec{U}_{\mathrm{ls}}$ denote the large-scale SSH and wind and the tilde $\widetilde{\mathrm{SSH}}$ and $\widetilde{\vec{U}}$ represent a 12-month running mean.

Trends, significance and uncertainties. All the linear trends are calculated by applying a linear least-squares regression model to the spatially integrated time series and statistically tested using a modified Mann–Kendall test[11,55]. The trends with a P value <0.05 are considered statistically significant. The uncertainties of trends correspond to the standard error, which is the standard deviation of the time series divided by the square root of the effective sample size from the Mann–Kendall test.

Data availability

The satellite altimetry products from AVISO were produced by Ssalto/Duacs and distributed by EU Copernicus Marine and Environment Monitoring Service and can be found at https://resources.marine.copernicus.eu/product-detail/SEALEVEL_GLO_PHY_L4_MY_008_047. The SST products OISST v.2.1 can be downloaded from https://www.ncei.noaa.gov/products/optimum-interpolation-sst. The BRAN2016 and BRAN2020 reanalysis are provided by CSIRO Australia and available at https://research.csiro.au/bluelink/outputs/data-access/. Ocean surface winds were taken from ECMWF's ERA5 reanalysis product and can be accessed at https://doi.org/10.24381/cds.f17050d7. The SAM index[56] was downloaded from http://lijianping.cn/dct/attach/Y2xiOmNsYjpBU0NJSTo4NjQ=.

Code availability

The SAM index and all Jupyter Notebook scripts used for producing the figures will be available in the github repository (https://github.com/lijunde/WBCs_SST_EKE) and publicly available in the figshare[57] (https://doi.org/10.6084/m9.figshare.20473941.v1).

References

53. Kang, D. & Curchitser, E. N. Energetics of eddy-mean flow interactions in the Gulf Stream region. *J. Phys. Oceanogr.* **45**, 1103–1120 (2015).
54. Halo, I. et al. Mesoscale eddy variability in the southern extension of the East Madagascar Current: seasonal cycle, energy conversion terms, and eddy mean properties. *J. Geophys. Res. Oceans* **119**, 7324–7356 (2014).
55. Yue, S. & Wang, C. The Mann–Kendall test modified by effective sample size to detect trend in serially correlated hydrological series. *Water Resour. Manag.* **18**, 201–218 (2004).
56. Nan, S. & Li, J. The relationship between the summer precipitation in the Yangtze River valley and the boreal spring Southern Hemisphere annular mode. *Geophys. Res. Lett.* **30**, 2266 (2003).
57. Li, J., Roughan, M. & Kerry, C. WBCs_SST_EKE. Software. *figshare* https://doi.org/10.6084/m9.figshare.20473941.v1 (2022).

Author contributions

M.R. and J.L. conceived the study and developed the conceptual framework. J.L. conducted the analysis and wrote the first draft. M.R., J.L. and C.K. contributed to interpreting the results, writing and editing the manuscript.

Competing interests

The authors declare no competing interests.

Additional information

Extended data is available for this paper at https://doi.org/10.1038/s41558-022-01473-8.

**Correspondence and requests for materials** should be addressed to Junde Li or Moninya Roughan.

Peer review information *Nature Climate Change* thanks Helene Hewitt, Dujuan Kang and the other, anonymous, reviewer(s) for their contribution to the peer review of this work.

**Reprints and permissions information** is available at www.nature.com/reprints.
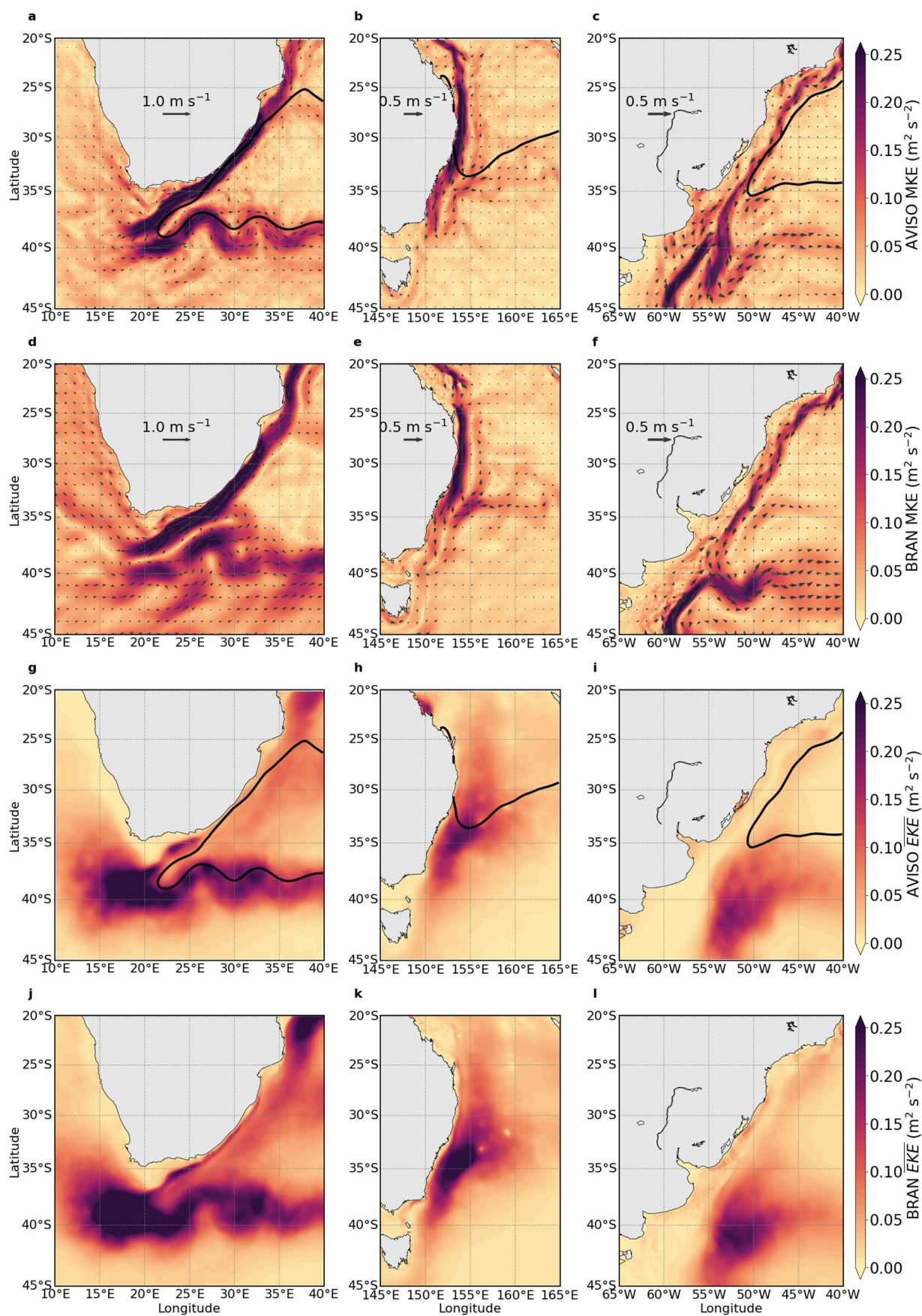
Extended Data Fig. 1 | See next page for caption.

Extended Data Fig. 1 | Surface MKE and mean surface EKE over the 28-year (1993–2020) from AVISO and BRAN in the SH WBCs. a, Spatial distribution of surface MKE in the AC system. The grey vectors indicate surface geostrophic velocities. The black line indicates the 0.9 m contour of climatological mean SSH (1993–2020) from AVISO. **b,c**, Same as **a**, but for the EAC and BC, respectively. The black line in **c** indicates the 0.6 m contour of climatological mean SSH from AVISO. **d–f**, Same as **a–c**, but for the surface MKE from BRAN. **g–l**, Same as **a–c**, but for the mean surface EKE from AVISO (**g–i**) and BRAN (**j–l**), respectively.
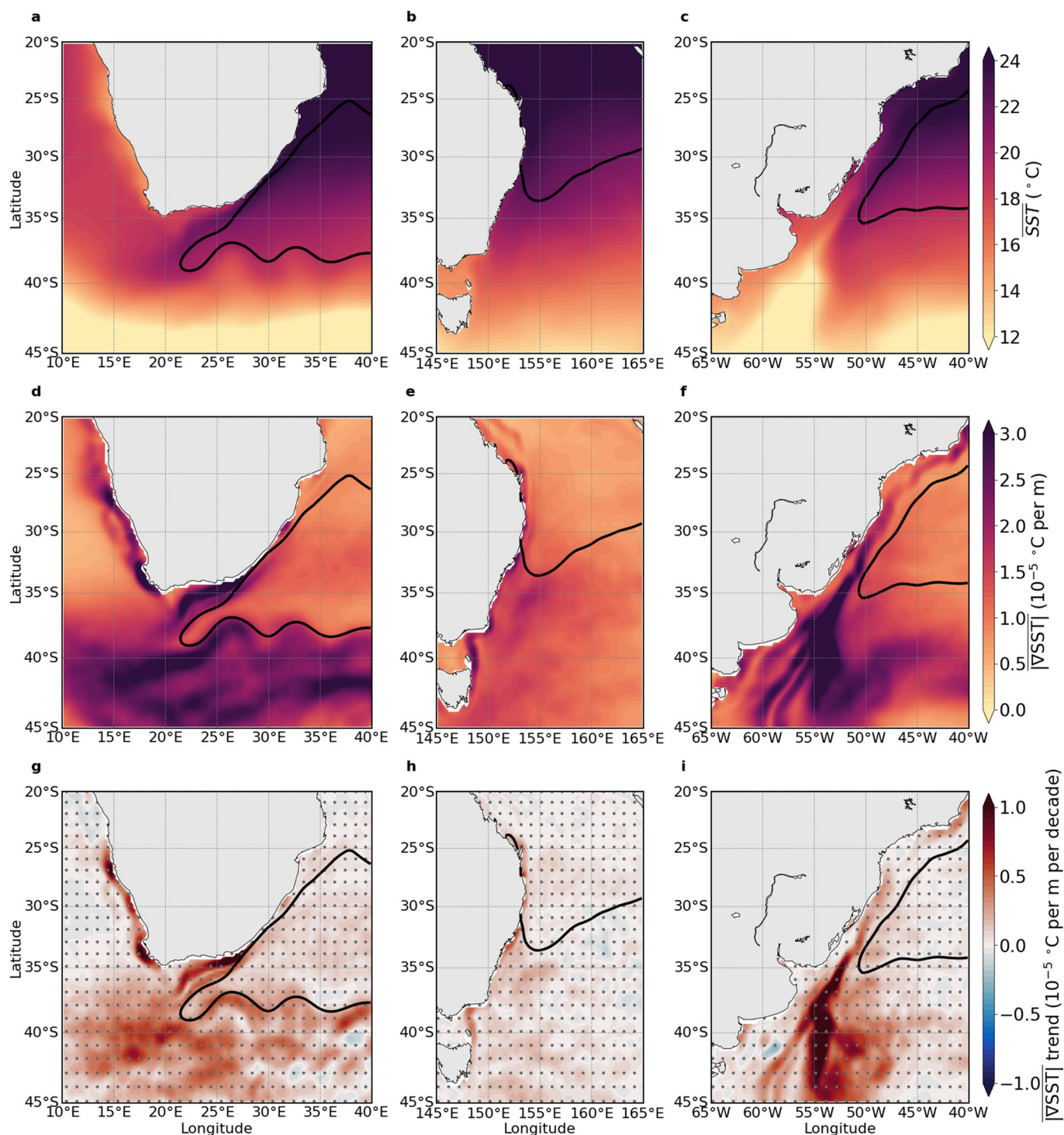
Extended Data Fig. 2 | Observed mean SST, mean SST gradient magnitude and trends of SST gradient magnitude in the SH WBCs. a, Spatial distribution of mean SST in the AC system. The black line indicates the 0.9 m contour of climatological mean SSH (1993–2020) from AVISO. **b–c**, Same as **a**, but for the EAC and BC, respectively. The black line in **c** indicates the 0.6 m contour of climatological mean SSH from AVISO. **d–f**, Same as **a–c**, but for the mean SST gradient magnitude. **g–i**, Same as **a–c**, but for the trends of SST gradient magnitude.
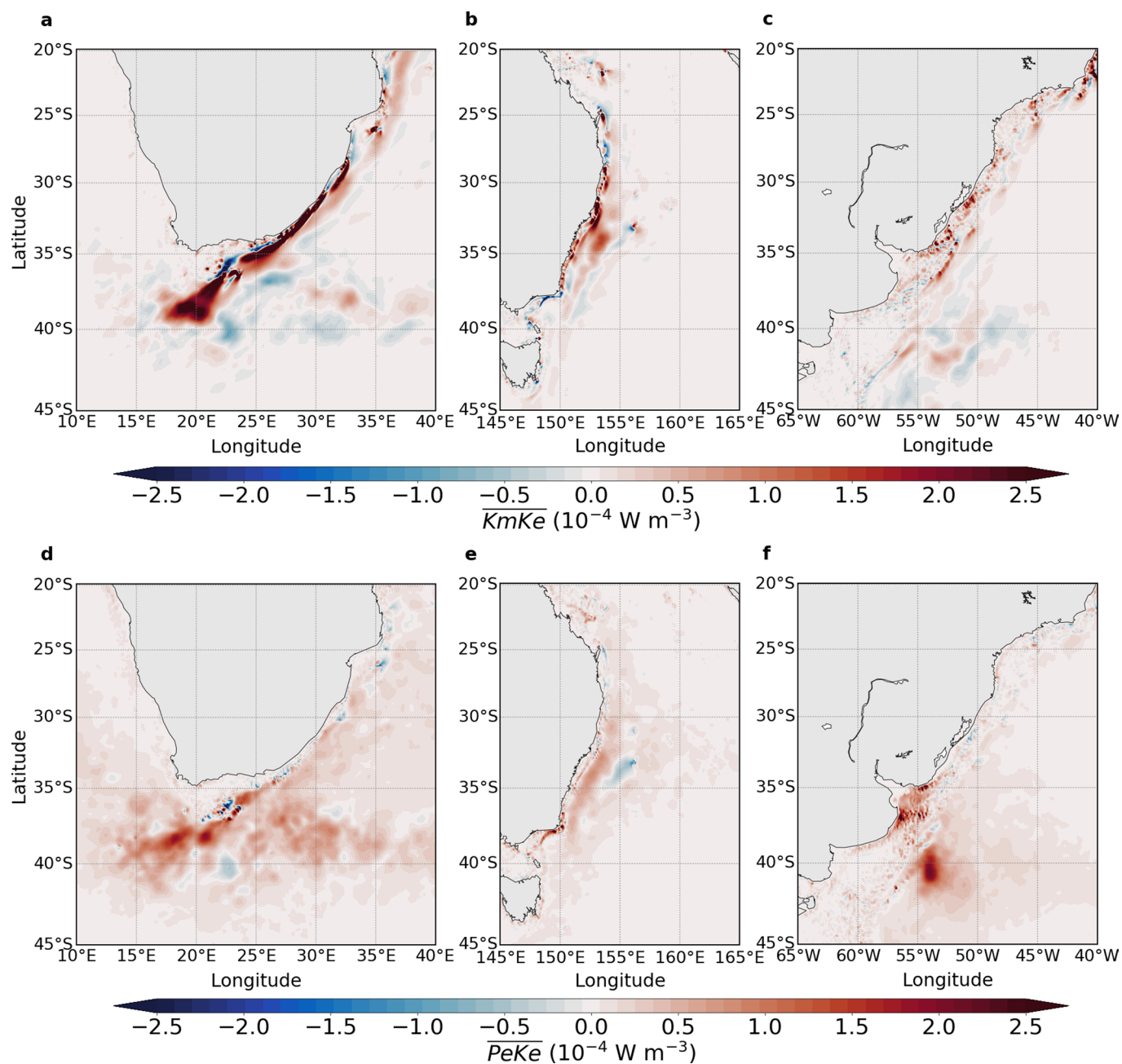
Extended Data Fig. 3 | Mean KmKe and PeKe from BRAN over the upper 1000 m in the SH WBCs. a, Spatial distribution of mean KmKe in the AC system. **b–c**, Same as **a**, but for the EAC and BC system, respectively. **d–f**, Same as **a–c**, but for the mean PeKe.